Geophysical Research Letters

RESEARCH LETTER
10.1029/2023GL102740

Strong Effect of Stress on the Seismic Signature of the Post-Stishovite Phase Transition in the Earth's Lower Mantle

Biao Wang[1], Johannes Buchen[1], Alba San José Méndez[2], Alexander Kurnosov[3], Giacomo Criniti[3], Hanns-Peter Liermann[2], and Hauke Marquardt[1]

[1]Department of Earth Sciences, University of Oxford, Oxford, UK, [2]Deutsches Elektronen-Synchrotron DESY, Hamburg, Germany, [3]Bayerisches Geoinstitut, University of Bayreuth, Bayreuth, Germany

Key Points:

- Continuous compression experiments were performed to study the post-stishovite phase transition under different stress conditions
- Deviatoric stresses shift the phase transition to a shallower depth in the lower mantle
- The bulk modulus of sintered polycrystalline stishovite differs from that of stishovite powder and drops at the phase transition

Supporting Information:

Supporting Information may be found in the online version of this article.

Correspondence to:

B. Wang,
biao.wang@earth.ox.ac.uk

Citation:

Wang, B., Buchen, J., Méndez, A. S. J., Kurnosov, A., Criniti, G., Liermann, H.-P., & Marquardt, H. (2023). Strong effect of stress on the seismic signature of the post-stishovite phase transition in the Earth's lower mantle. *Geophysical Research Letters*, *50*, e2023GL102740. https://doi.org/10.1029/2023GL102740

Received 10 JAN 2023
Accepted 3 MAY 2023

Abstract The stishovite to post-stishovite phase transition may modify the scattering of seismic waves by stishovite-bearing rocks in the Earth's lower mantle. A series of continuous compression experiments on sintered polycrystalline stishovite was performed to study the effect of stress on the phase transition. The experimental results show that the phase transition shifts to lower pressures as the magnitude of deviatoric stress increases. Our results further show that the bulk modulus of sintered polycrystalline stishovite differs from that derived from single crystal measurements and decreases at the phase transition. In cold regions, such as subducted slabs, stresses may accumulate and shift the phase transition to a shallower depth. In hot regions with less stress, such as rising plumes, the phase transition is shifted to a greater depth. In addition, the phase transition may have varying seismic signatures depending on the behavior of the grain boundaries in mantle rocks and the micro-stresses present in neighboring grains.

Plain Language Summary Stishovite and post-stishovite are high-pressure polymorphs of SiO_2 that are stable in the Earth's lower mantle. The stishovite to post-stishovite phase transition may affect the way seismic waves travel through mantle rocks. To detect SiO_2 phases in the deep mantle, it is essential to investigate the depth of the phase transition and its effects on seismic wave propagation. Experiments were conducted to simulate the high-pressure environment of the lower mantle and to study the phase transition of sintered polycrystalline stishovite aggregates, in which crystals are firmly connected to each other. Our study finds that the phase transition is sensitive to deviatoric stress, which is a measure of the directional stress difference. An increase in deviatoric stresses shifts the phase transition to shallower depths in the mantle. We further find that at pressures below the phase transition, sintered polycrystalline stishovite aggregates exhibit lower compressibility compared to stishovite powder and single crystals, but the compressibility increases abruptly at the phase transition, probably caused by grain-grain interactions in the sintered samples. Therefore, the behavior of seismic waves will be different when passing through stishovite-bearing rocks with different degree of grain-grain interactions, particularly under conditions close to the phase transition boundary.

1. Introduction

SiO_2 stishovite is expected to constitute 20–25 vol.% of subducted metamorphosed Mid-Ocean Ridge Basalt (MORB) in the Earth's lower mantle (Hirose et al., 2005; Ishii et al., 2022). SiO_2-rich domains with excess SiO_2 in the form of stishovite may also have formed by partial melting of bridgmanite-rich rocks or by the crystallization of a magma ocean in the lower mantle (Amulele et al., 2021; Boujibar et al., 2016). Additionally, according to geophysical and geochemical models, SiO_2 may have exsolved from the Earth's liquid outer core and dispersed throughout the lower mantle by convection (Helffrich et al., 2018; Hirose et al., 2017). Therefore, understanding the physical properties of solid SiO_2 phases under lower mantle conditions is essential for understanding geodynamic processes such as deep subduction of oceanic crust and convective dispersal of silica-rich rocks as well as quantifying the abundance of SiO_2 in the deep mantle.

An important feature of SiO_2 in the lower mantle is the phase transition from stishovite to post-stishovite, which modifies the scattering of seismic waves by stishovite-bearing rocks such as deeply subducted and metamorphosed MORB (Buchen, 2021; Kaneshima & Helffrich, 2010; Marquardt & Thomson, 2020). Experimental and theoretical studies on crystalline SiO_2 polymorphs have shown that the tetragonal crystal structure of stishovite (space group: $P4_2/mnm$) distorts to the orthorhombic high-pressure polymorph post-stishovite (space group: $Pnnm$) at around 55 GPa at room temperature and under quasi-hydrostatic conditions (e.g., Andrault et al., 1998).

Since the transition pressure increases with temperature (Fischer et al., 2018; Nomura et al., 2010), pure SiO_2 is expected to transform from stishovite to post-stishovite at depths in excess of 1,500 km in the lower mantle, deeper than many of the observed seismic S-wave scatterers that are usually related to the post-stishovite phase transition (Kaneshima, 2019). Some previous studies have suggested that chemical impurities such as aluminum (Al) and H_2O may counteract the thermal effect and decrease the phase transition pressure (Lakshtanov et al., 2007; Zhang et al., 2022). However, while the Al content in stishovite may range from 0 to 1.5 mol% (Hirose et al., 2005; Ishii et al., 2019; Litasov & Ohtani, 2005), stishovite in diamond inclusions contains very small amounts of impurities (Wirth et al., 2007).

The post-stishovite phase transition is a second-order displacive structural phase transition (Andrault et al., 1998; Carpenter et al., 2000) and should therefore be very sensitive to deviatoric stress (Asahara et al., 2013; Shieh et al., 2002; Singh et al., 2012). By including stresses into the Landau expansion for the phase transition (Carpenter, 2007; Carpenter et al., 2000), it can be shown that deviations from a hydrostatic stress state may change the equilibrium pressure and temperature of the phase transition. Geodynamic modeling combined with seismic observations of deep earthquakes indicates that deviatoric stresses of up to 400 MPa may build up in cold subducting slabs (Kirby et al., 1996; Čížková et al., 2020). Even larger deviatoric stresses may arise at the grain scale from interactions between strong and weak minerals (Girard et al., 2016; Thielmann et al., 2020), for example, in subducted oceanic crust (Immoor et al., 2022). Understanding the effect of deviatoric stress on the phase transition pressure is thus pivotal to determine the depth of the phase transition and infer the presence of free SiO_2 phases in the lower mantle from the observation of seismic scatterers. However, the effects of deviatoric stress on the post-stishovite phase transition remain largely unconstrained. Asahara et al. (2013) reported a phase transition pressure of 25–35 GPa in a diamond-anvil cell (DAC) compression experiment using NaCl as Pressure Transmitting Medium (PTM) while Singh et al. (2012) reported a phase transition pressure of 44 $\pm$ 8 GPa in a DAC compression experiment without any PTM, that is, in the presence of presumably larger deviatoric stress. Although both studies suggest an effect of deviatoric stress on the phase transition pressure, the magnitude of this effect is poorly quantified.

In addition to constraining the depth of the post-stishovite phase transition, the related impact on elastic properties must be considered when interpreting observations of seismic scatterers (Kaneshima, 2019; Kaneshima & Helffrich, 2010). Previous studies showed a substantial softening of stishovite's shear modulus (G) across the phase transition but reported conflicting results on the behavior of the bulk modulus (K). Carpenter et al. (2000) analyzed previous experimental data using Landau theory and predicted that the phase transition may lead to a substantial softening of G with only a small effect on K. Yang and Wu (2014) investigated the elasticity of stishovite and post-stishovite using first-principles simulations and found a sharp decrease in G and a very small decrease in K. Zhang et al. (2021) studied the elasticity of stishovite and post-stishovite single crystals using Brillouin spectroscopy, impulsive stimulated light scattering, Raman spectroscopy, and X-ray diffraction (XRD) and found that the phase transition can lead to substantial softening of G together with a very weak effect on K. In contrast, Buchen et al. (2018) used Landau theory applied to experimental XRD data on sintered polycrystalline stishovite and predicted a significant and sharp reduction of K in addition to the gradual softening of G. The different behavior of K in different studies may be caused by differences in the microstructure of different samples, including grain size and the behavior of grain boundaries, as well as by different stress states.

To constrain the effect of the stress state on the post-stishovite phase transition pressure and better understand the behavior of K, we performed a series of continuous compression experiments on sintered polycrystalline stishovite samples under different stress conditions in combination with time-resolved XRD. By recording hundreds of XRD patterns in a single experimental run, we obtained quasi-continuous pressure-volume ($P(V)$) data sets. The dense pressure coverage allows us to calculate K by numerical differentiation of the $P(V)$ data without invoking further assumptions (Marquardt et al., 2018; Méndez et al., 2022).

2. Materials and Methods

The sintered polycrystalline stishovite samples used in this study were synthesized in a large-volume press at 15 GPa and 1,573 K using pure silica glass rods as the starting material. The average grain size of the samples was determined to be about 0.2 μm. More details on sample characterization can be found in previous studies (Buchen et al., 2018; Nishiyama et al., 2015). The synthesized sample was first mechanically polished into plane-parallel thin sections with a final thickness of about 10 μm and then cut into pieces with a diameter of

Table 1
Summary of Four Continuous Compression Experiments

Run number	PTM	DAC type	Compression type[a]	Detector	Pressure range
run#1	Ne	dDAC	Ramp	LAMBDA	30–80 GPa
run#2	Ne	mDAC	Ramp	PE	5–39 GPa
run#3	No PTM	mDAC	Ramp	PE	13–45 GPa
run#4	Ne	dDAC	Sinusoidal	PE	35–73 GPa

Note. PTM: Pressure Transmitting Medium, Ne: Neon, LAMBDA: LAMBDA detector, PE: PerkinElmer detector.

[a]Details about compression type can be found in Figure S2 in Supporting Information S1.

about 40 μm using a focused ion beam (Marquardt & Marquardt, 2012) or broken mechanically. Rhenium gaskets were pre-indented to a thickness of about 30 μm in a symmetric DAC using diamonds with 200 μm culets. Holes with diameters of about 150 μm were laser-drilled into the gaskets. Given the small amount of sample used in DAC experiments and the relatively low-Z character of stishovite in comparison to rhenium, a ring of amorphous metallic glass with the chemical composition of $Fe_{0.79}Si_{0.07}B_{0.14}$ was placed inside the rhenium gasket hole to avoid parasitic diffraction from the rhenium gasket (Dong et al., 2022; Méndez et al., 2020). The outer and inner diameters of the rings were approximately 130 and 80 μm, respectively. Gold (Au) powder was loaded on top of the stishovite sample for pressure determination. An optical image of the DAC sample chamber is shown in Figure S1 in Supporting Information S1.

Time-resolved XRD experiments in dynamic (piezo-driven) Diamond Anvil Cells (dDAC) and membrane-driven Diamond Anvil Cells (mDAC) were conducted at the Extreme Conditions Beamline P02.2 at PETRA III, Hamburg, Germany (Liermann et al., 2015). A detailed description of dDAC and mDAC setup can be found in Supporting Information S1. Four continuous compression experiments were performed at room temperature, including two dDAC experiments and two mDAC experiments. Table 1 summarizes the pressure ranges and other details of the experiments. Neon (Ne) was used as PTM in run#1, run#2, and run#4, while no PTM was used in run#3. Therefore, run#3 was expected to create larger deviatoric stress. The stress states in run#1 and run#2 were comparable because their experimental conditions were similar. In addition to using Ne as PTM, sinusoidal compression cycles were applied in run#4 using a dDAC to achieve a different stress condition from run#1 and run#2.

Two-dimensional XRD patterns were integrated into 2θ-intensity profiles using DIOPTAS (version win 0.50, Prescher & Prakapenka, 2015). Data quality details can be found in Figures S2 and S3 in Supporting Information S1. A customized peak-fitting script was written in Python to analyze the continuous series of time-resolved XRD profiles (Wang, 2022). The peak positions obtained from fitting were used to calculate the unit cell parameters of stishovite and gold (Au). The difference between the unit cell parameters obtained from peak positions and Le Bail refinement in GSAS-II (Toby & Von Dreele, 2013) is smaller than 0.5% (Figure S4 in Supporting Information S1). The pressures in the experiment were calculated from the derived unit cell volumes of Au using the Equation of State (EoS) parameters of Fei et al. (2007). The isothermal bulk moduli (K_T) of stishovite and post-stishovite were directly calculated from our nearly continuous $P(V)$ data based on the definition $K_T = -V \times (\partial P/\partial V)_T$ (Marquardt et al., 2018; Méndez et al., 2021, 2022).

Deviatoric stresses and micro-stresses were derived using the line-shift (Singh et al., 1998; Singh & Kenichi, 2001) and the line-width (Singh, 2004) methods, respectively. Deviatoric stress calculated from the line-shift method corresponds to the difference between the maximum stress (usually along the compression direction) and the minimum stress (usually along the radial direction) inside the pressure chamber of the DAC. This method is limited to materials with cubic crystal symmetry (Singh & Kenichi, 2001). We, therefore, calculated the deviatoric stresses for Au and Ne when enough peaks could be fitted (i.e., Au in run#1 and Ne in run#4) (Figures S2 and S3 in Supporting Information S1). In the experiments where Ne was used as PTM and Au was loaded on top of the sample, Au and the sample were surrounded by Ne (Figure S1 in Supporting Information S1), and the deviatoric stresses derived from Au and/or Ne are expected to reflect the deviatoric stresses imposed on the stishovite samples. In experiments without PTM (run#3), the strength of stishovite from previous studies (Shieh et al., 2002; Singh et al., 2012) was used to estimate the upper limit of the deviatoric stress applied to the stishovite sample.

Micro-stress calculated from the line-width method reflects the differences between maximum and minimum stresses acting on the individual grains in a polycrystalline aggregate. As micro-stresses arise from the imposed deviatoric stress, their magnitudes are expected to be smaller than the magnitudes of the deviatoric stress. At least three diffraction lines are needed to obtain meaningful estimates of micro-stress. When calculating the micro-stresses in stishovite for run#2–4, we used recently published elastic coefficients (Zhang et al., 2021) together with our measurements of line-widths of relevant reflections at ambient conditions to correct for instrumental line broadening.

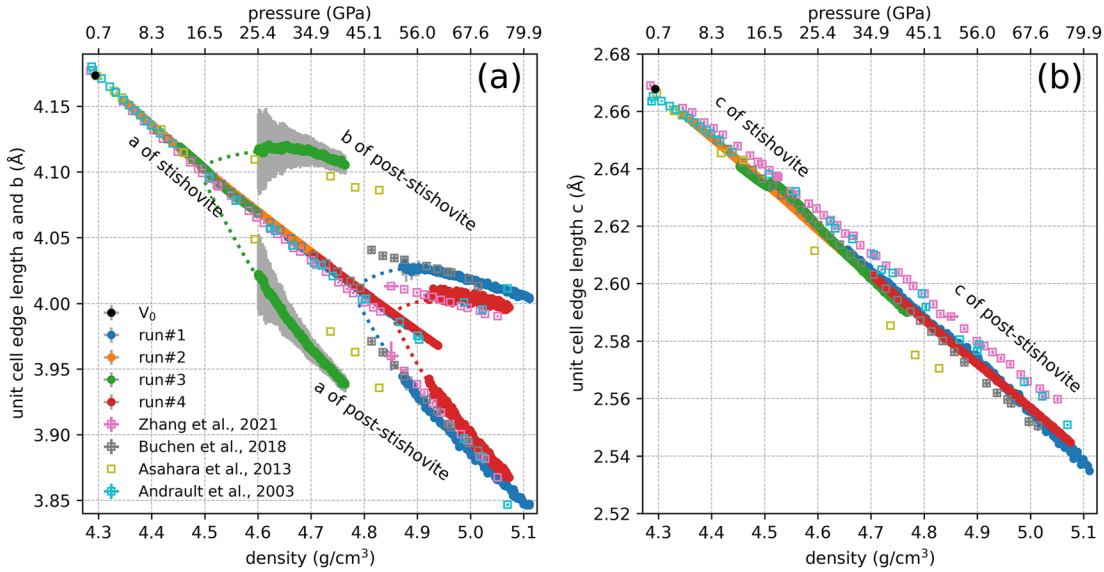

Figure 1. Unit cell parameters of stishovite and post-stishovite as a function of density (primary axis) and pressure (secondary axis) measured in this study (solid circles) and previous studies (open squares). Pressures for all data in the figure were recalculated using the equation of state of stishovite determined by Andrault et al. (2003). The dashed lines for runs #1, #3, and #4 are interpolated guidelines to illustrate the evolution of a- and b-axes of post-stishovite close to the phase transition. Zhang et al. (2021) used stishovite single crystals. Asahara et al. (2013) used sintered polycrystalline stishovite, and Andrault et al. (2003) used stishovite powder. Buchen et al. (2018) used the same sintered polycrystalline stishovite as in the present study. For more details on the unit cell edge lengths of runs#1–4, see Figures S4–S7 in Supporting Information S1.

3. Results and Discussion

Figure 1 shows the unit cell parameters of stishovite and post-stishovite as a function of density and pressure for this study and selected previous works (Andrault et al., 2003; Asahara et al., 2013; Buchen et al., 2018; Zhang et al., 2021). We plotted the unit cell parameters of stishovite and post-stishovite against their densities on the primary axis to better compare different studies using different pressure standards and to minimize the effect of deviatoric stress on the accuracy of the pressure determination. For the same reasons, all pressures in Figure 2 were recalculated using the reported unit cell volumes of each study and the EoS parameters for stishovite as given by Andrault et al. (2003).

At ambient conditions, the *a*- and *c*-axes of our sintered polycrystalline stishovite are comparable to those reported in previous studies. At high pressures, prior to the phase transition, the *a*- and *c*-axes of sintered polycrystalline stishovite from this study and previous studies (Asahara et al., 2013; Buchen et al., 2018) are consistent with each other despite the different PTM used. The *a*-axes of sintered polycrystalline stishovite are systematically larger than those of stishovite powder (Andrault et al., 2003) and single crystals (Zhang et al., 2021), while the *c*-axes are systematically smaller. As suggested earlier (Buchen et al., 2018), this might be related to grain-grain interactions across stiff grain boundaries in the sintered samples, which may cause the unit cell to compress differently.

In run#3, stishovite transforms to post-stishovite at a substantially lower pressure than in runs#1 and #4. Asahara et al. (2013) observed qualitatively similar results when compressing sintered polycrystalline samples in NaCl PTM, although they only presented three data points above 30 GPa. The unit cell parameters of the experiments using Ne PTM (run#1, run#2, and run#4) are close to those from previous studies under quasi-hydrostatic conditions (Andrault et al., 2003; Buchen et al., 2018; Zhang et al., 2021). The slight difference between run#1 and run#4 is likely caused by minor differences in stress conditions.

Figure 2a shows the square of the symmetry-breaking spontaneous strain $(e_1 - e_2)^2 = \left(\left(a_{pSt} - b_{pSt}\right)/a_{St}\right)^2$ arising from the phase transition (Carpenter et al., 2000) as a function of pressure in comparison to previous studies (Andrault et al., 2003; Asahara et al., 2013; Buchen et al., 2018; Zhang et al., 2021), where a_{pSt} and b_{pSt} are the *a*- and *b*-axes of the post-stishovite, respectively, and a_{St} is the *a*-axis of stishovite extrapolated into the stability field of post-stishovite. $a_{St} = \left(a_{pSt} \times b_{pSt}\right)^{0.5}$ is used in this study because the volume strain of the phase transition is small (Carpenter et al., 2000). The intersection of the linear relation between the squared symmetry-breaking

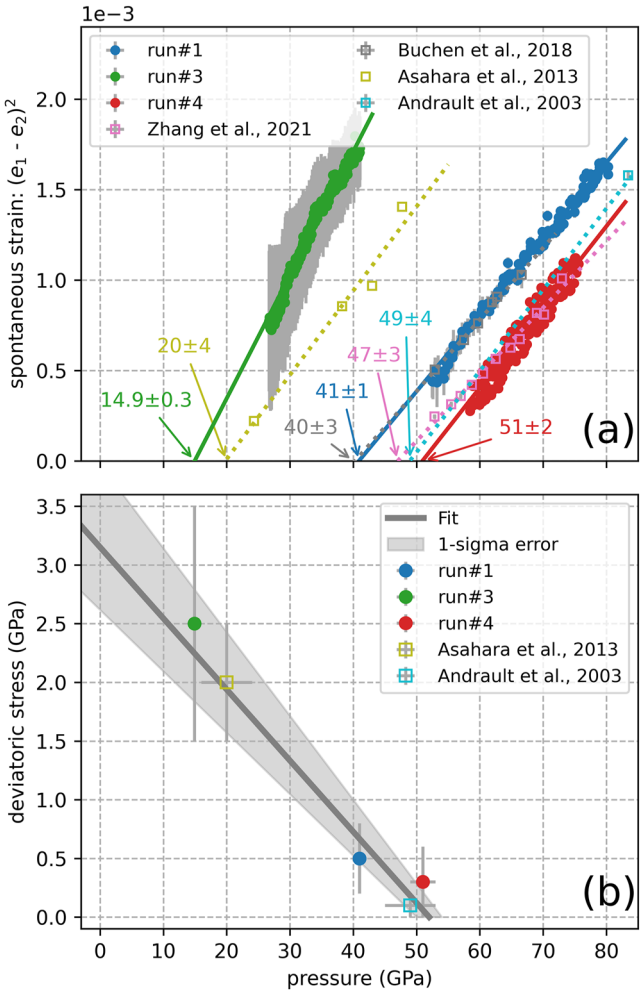

Figure 2. Effect of deviatoric stress on the post-stishovite phase transition. (a) Square of the symmetry-breaking spontaneous strain as a function of pressure as measured in this study (solid circles and lines) and reported previously (open squares and dashed lines) (Andrault et al., 2003; Asahara et al., 2013; Buchen et al., 2018; Zhang et al., 2021). Lines show linear fits to each data set. Data close to the phase transition were not included for fitting. (b) Effect of deviatoric stress on the pressure of the post-stishovite phase transition. The deviatoric stress in Asahara et al. (2013) is estimated from the pressure distribution in the sample chamber obtained using the NaCl-B2 pressure gauge; the uncertainty of the stress is assumed to be 0.5 GPa. The deviatoric stress in Andrault et al. (2003) is assumed to be 0.1 ± 0.1 GPa because the stress was released by laser heating. The gray line shows the estimated linear effect of deviatoric stress on the phase transition pressure. The gray band shows the 1-sigma error of the linear fitting. In the absence of deviatoric stress, the phase transition pressure is estimated to be 52 ± 2 GPa.

spontaneous strain and the pressure axis at $(e_1 - e_2)^2 = 0$ provides an estimate of the phase transition pressure. The phase transition pressure in run#4 is determined to be 51 ± 2 GPa. The phase transition pressure in run#1 is determined to be 41 ± 1 GPa, lower than in Andrault et al. (2003) and Zhang et al. (2021) but close to Buchen et al. (2018). The phase transition pressure in run#3 is determined to be 14.9 ± 0.3 GPa. A visualization of the phase transition in run#1 is provided in Movie S1.

Because Ne PTM surrounded the sample, the deviatoric stresses in Ne should reflect the deviatoric stresses imposed on stishovite in run#4. Because Au was loaded on top of the sample (Figure S1 in Supporting Information S1), and the calculated deviatoric stresses in Au are much lower than its flow strengths (Singh et al., 2006), the deviatoric stress in Au should reflect the deviatoric stresses imposed on the stishovite in run#1. Therefore, deviatoric stresses in run#1 and run#4 at the phase transition are estimated from Ne and Au to be 0.5 ± 0.3 GPa and 0.3 ± 0.3 GPa, respectively (Figure S8 in Supporting Information S1). Because no PTM was used in run#3, the maximum deviatoric stresses that the stishovite sample can experience equals the flow strength of stishovite. Therefore, the deviatoric stress in stishovite in run#3 at 14.9 GPa is estimated to be 2.5 ± 1 GPa according to previous strength studies based on radial XRD experiments (Shieh et al., 2002; Singh et al., 2012).

Figure 2b shows the relationship between deviatoric stress and the resulting shift in the phase transition pressure. A linear approximation is derived from available data: $P_{tr}(t) = P_0 + (b \times t)$, where $P_0 = 52 \pm 2$ GPa is the phase transition pressure of pure SiO_2 stishovite at room temperature and under hydrostatic conditions, $b = -16.5 \pm 2.5$ is the factor describing the effect of the deviatoric stress, and t is the magnitude of deviatoric stress in GPa. Because the deviatoric stress in run#3 is an upper limit estimation, the equation provides a lower bound for the effect of deviatoric stress.

If 500 MPa of deviatoric stress is applied to stishovite, the phase transition pressure will be decreased by 8.3 ± 1.3 GPa. This pressure difference would correspond to about 250 km depth difference in the lower mantle. The effect of 500 MPa deviatoric stress is comparable to the effect of a 500 K temperature difference (Fischer et al., 2018) or a 0.3 mol% Al impurity difference (Zhang et al., 2022). It is worth noting that the effects of temperature and deviatoric stress likely amplify each other since regions of lower temperatures are often correlated with regions of larger deviatoric stress. Stishovite in cold subducting slabs might thus transform to post-stishovite at a shallower depth than in warm subducting slabs. If not directly linked to subduction events, stishovite would likely transform even deeper in the lower mantle as a result of higher temperatures and lower deviatoric stresses. We emphasize that the magnitude of the effect of deviatoric stress is a conservative estimate as the effect appears more pronounced when considering micro-stresses (a shift of about 40 GPa for a micro-stress difference of 500 MPa, Figure S9 in Supporting Information S1).

Considering the combined effects of temperature, deviatoric stress, and chemical impurities (such as Al and H_2O), the post-stishovite phase transition in cold slabs (lower temperature and larger stress) should occur at shallower depths than in warm slabs (higher temperature and smaller deviatoric stress). For SiO_2 exsolved from the outer core, the post-stishovite phase transition is expected in deeper parts of the lower mantle (very high temperature, very small stress, and minor chemical impurities). To estimate the range of possible phase transition depths in the lower mantle, we assume that the effects of temperature (Fischer et al., 2018), Al impurity (Zhang et al., 2022), and deviatoric stress can be combined by linear superposition. For stishovite in the metabasaltic fraction of a cold

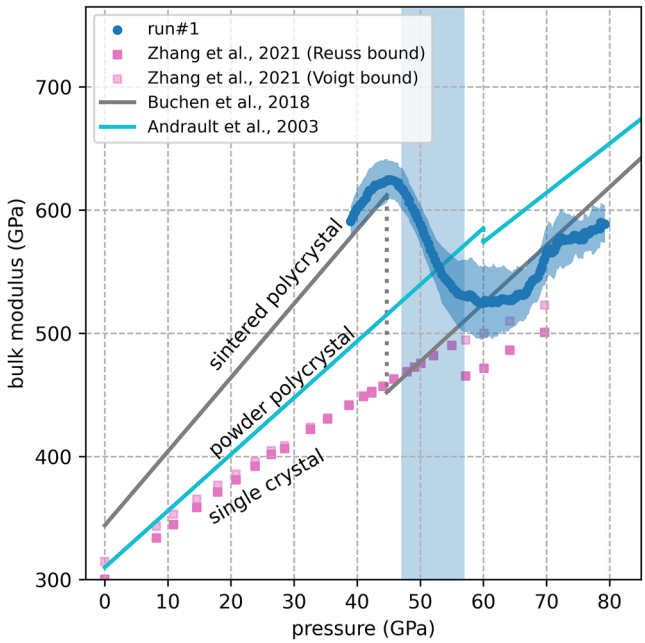

Figure 3. Bulk moduli (K) of sintered polycrystalline stishovite across the stishovite to post-stishovite phase transition derived for run#1. The solid blue dots show K of sintered polycrystalline stishovite calculated from numerical differentiation of our quasi-continuous $P(V)$ data. The solid gray line shows K of sintered polycrystalline stishovite predicted using Landau theory by Buchen et al. (2018). The solid cyan line shows K of stishovite powder determined using the Equation of State fit by Andrault et al. (2003). The pink and light pink dots are the Reuss and Voigt bounds for the K of single-crystal stishovite calculated using the elastic constants reported by Zhang et al. (2021).

slab, the temperature could be 500 K lower than in the surrounding mantle (Tan et al., 2002), the stishovite may contain up to 0.5 mol.% Al impurities (Ishii et al., 2019), and the deviatoric stress may reach 500 MPa at the grain scale. In this scenario, the phase transition should occur at a depth of around 1,300 km in the lower mantle. Because our estimation of the stress effect is a lower bound, the phase transition might be shifted to even shallower depths. In a warm slab, the temperature may equilibrate with the surrounding mantle and anneal deviatoric stresses. Consequently, the post-stishovite phase transition should occur at a depth of around 1,700 km if the stishovite contains 0.5 mol.% Al impurities. For silica exsolved from the outer core and rising through the mantle with plumes (Helffrich et al., 2018), temperatures might be even higher than in the surrounding mantle, shifting the post-stishovite phase transition to depths in excess of 2,000 km for pure SiO_2.

Along with the phase transition depth, an understanding of the seismic signature of the post-stishovite phase transition is needed to prospect for stishovite-bearing rocks, such as metabasalt, in the Earth's lower mantle. In addition to the widely reported decrease in G (Asahara et al., 2013; Carpenter et al., 2000; Yang & Wu, 2014; Zhang et al., 2021), an anomalous behavior of K is observed in our study. Figure 3 shows that K of sintered polycrystalline stishovite reaches a value of 520 GPa before the phase transition, which is about 40% higher than K derived from single-crystal measurements on stishovite (Zhang et al., 2021). Additionally, K decreases by about 25% at the phase transition, thereby confirming the decrease of K for sintered polycrystalline samples as previously predicted by Buchen et al. (2018).

The compression behavior of sintered polycrystalline stishovite along different crystallographic axes deviates from that of stishovite powder and single crystals (Figure 1). The reduced compressibility of the sintered polycrystalline stishovite (Figure 3) suggests that the overall compression behavior is dominated by the stiffest crystallographic direction, acting as a rigid framework. When a stiff crystallographic direction of one grain coincides with a softer direction of the neighboring grain along the shared grain boundary, the stiff axis might dominate the overall compression behavior in this direction. In three dimensions, such grain-grain interactions across the grain boundaries may therefore shift the overall compression behavior toward that of the least compressible direction. The mismatch in the compression behavior of neighboring, differently oriented grains will simultaneously lead to a build-up of micro-stresses in the grains, which cannot be relaxed by grain boundary movements in the sintered sample. At the displacive phase transition, grains have the flexibility to distort and to reduce the mismatch with neighboring grains, and hence release micro-stresses. In combination with the perturbation of the elastic constants at the post-stishovite phase transition (e.g., Zhang et al., 2021), this may explain the observed drop in bulk modulus at the phase transition.

The compression behavior of the sintered polycrystalline stishovite might change with the average grain size as grain size could affect the build-up of stresses across grain boundaries where differently-orientated neighboring grains meet. We note, however, that our results are unlikely to be dominated by grain boundary effects that become significant for nanocrystalline materials which usually lead to elastic softening. Experiments on nanocrystalline MgO, for example, showed that elastic properties are affected by grain boundaries for grain sizes well below 100 nm and that such small grain sizes result in a softening of elastic moduli (Marquardt, Gleason, et al., 2011; Marquardt, Speziale, et al., 2011; Yeheskel et al., 2005). Similar grain size limits for the transition to nano-behavior of a few tens of nanometers have been reported for quartz (McKnight et al., 2008) and derived numerically (Zhu & Zheng, 2010). With an average of 200 nm, the grain size of our sintered polycrystalline stishovite samples can be expected to be above the grain size limit for the transition to nano-behavior. However, more experiments are needed to constrain the effect of grain size on the elastic properties of sintered polycrystalline stishovite.

Depending on the behavior of the grain boundaries in mantle rocks, and the micro-stresses present in neighboring grains, the post-stishovite phase transition in slabs might be accompanied by a significant decrease of K due to the distortion of grains and possible weakening of the grain boundary network at the phase transition. The

resulting drop in the bulk modulus may then modify the v_P/v_S-ratio associated with stishovite-bearing rocks. This may explain why some seismic waves are scattered stronger in the shallow lower mantle than by deeper scatterers (Kaneshima, 2019; Kaneshima & Helffrich, 2010). While compression of sintered stishovite polycrystals to pressures of the lower mantle appears to preserve the locked character of grain boundaries and a framework of stiff axes, the behavior of grain boundaries at temperatures of the lower mantle and at frequencies of seismic waves remains largely unexplored and will be the subject of future experiments.

4. Conclusions

We quantified the effect of deviatoric stress on the post-stishovite phase transition pressure and determined the bulk modulus (K) of sintered polycrystalline stishovite samples across the phase transition. Deviatoric stresses act to decrease the phase transition pressure with a magnitude similar to the effects of temperature and aluminum impurities expected along typical geotherms and for rock compositions for the lower mantle. As a result, the post-stishovite phase transition is expected to occur at shallower depths in the lower mantle for stishovite-bearing rocks that experience substantial deviatoric stresses at comparably low temperatures, such as in cold subducted slabs. Grain-grain interactions may act to modify the compression behavior of sintered polycrystalline stishovite samples. Before the phase transition, the K of sintered polycrystalline stishovite is higher than that of single-crystal stishovite. We argue that the overall compression behavior of sintered stishovite is dominated by the compression behavior of the stiffest crystallographic direction, due to the presence of stiff grain boundaries that do not allow for sliding of grains past each other and prevent the release of micro-stresses. At the phase transition, the spontaneous distortion of grains may allow for relaxation and possibly weakening of the grain boundary network. The resulting drop of the bulk modulus is further amplified by the perturbation of elastic constants at the phase transition. Therefore, the seismic signature of stishovite-bearing rocks may differ in different regions of the lower mantle, depending on temperature, composition, stress, and possibly grain boundary behavior.

Data Availability Statement

All the data necessary to produce the results in this paper are available at https://doi.org/10.6084/m9.figshare.21859989.v3.

Acknowledgments
This research was supported by the European Union's Horizon 2020 research and innovation Programme (ERC Grant 864877). The experiments were performed at beamline P02.2(ECB) at PETRA III, DESY (Hamburg, Germany), a member of the Helmholtz Association HGF. We would like to thank Norimasa Nishiyama for sample synthesis, Raphael Njul for sample polishing, Konstantin Glazyrin and Mario Wendt for providing technical assistance at the beamline station, Niccolò Satta and Egor Koemets for helpful discussions and assistance with experiments, and Christian Plueckthun for helpful discussions on python coding. We would also like to thank Michael Carpenter and an anonymous referee for their constructive comments.

References

Amulele, G., Karato, S., & Girard, J. (2021). Melting of bridgmanite under hydrous shallow lower mantle conditions. *Journal of Geophysical Research: Solid Earth*, *126*(9), e2021JB022222. https://doi.org/10.1029/2021JB022222

Andrault, D., Angel, R. J., Mosenfelder, J. L., & Le Bihan, T. (2003). Equation of state of stishovite to lower mantle pressures. *American Mineralogist*, *88*(2–3), 301–307. https://doi.org/10.2138/am-2003-2-307

Andrault, D., Fiquet, G., Guyot, F., & Hanfland, M. (1998). Pressure-induced landau-type transition in stishovite. *Science*, *282*(5389), 720–724. https://doi.org/10.1126/science.282.5389.720

Asahara, Y., Hirose, K., Ohishi, Y., Hirao, N., Ozawa, H., & Murakami, M. (2013). Acoustic velocity measurements for stishovite across the post-stishovite phase transition under deviatoric stress: Implications for the seismic features of subducting slabs in the mid-mantle. *American Mineralogist*, *98*(11–12), 2053–2062. https://doi.org/10.2138/am.2013.4145

Boujibar, A., Bolfan-Casanova, N., Andrault, D., Bouhifd, M. A., & Trcera, N. (2016). Incorporation of Fe^{2+} and Fe^{3+} in bridgmanite during magma ocean crystallization. *American Mineralogist*, *101*(7), 1560–1570. https://doi.org/10.2138/am-2016-5561

Buchen, J. (2021). Seismic wave velocities in Earth's mantle from mineral elasticity. In H. Marquardt, M. Ballmer, S. Cottaar, & J. Konter (Eds.), *Mantle convection and surface expressions* (1st ed., pp. 51–95). American Geophysical Union. https://doi.org/10.1002/9781119528609.ch3

Buchen, J., Marquardt, H., Schulze, K., Speziale, S., Boffa Ballaran, T., Nishiyama, N., & Hanfland, M. (2018). Equation of state of polycrystalline stishovite across the tetragonal-orthorhombic phase transition. *Journal of Geophysical Research: Solid Earth*, *123*(9), 7347–7360. https://doi.org/10.1029/2018JB015835

Carpenter, M. A. (2007). Elastic anomalies accompanying phase transitions in (Ca,Sr)TiO_3 perovskites: Part I. Landau theory and a calibration for $SrTiO_3$. *American Mineralogist*, *92*(2–3), 309–327. https://doi.org/10.2138/am.2007.2295

Carpenter, M. A., Hemley, R. J., & Mao, H. (2000). High-pressure elasticity of stishovite and the $P4_2/mnm \rightleftharpoons Pnnm$ phase transition. *Journal of Geophysical Research*, *105*(B5), 10807–10816. https://doi.org/10.1029/1999JB900419

Čížková, H., Zahradník, J., Liu, J., & Bina, C. R. (2020). Geodynamic subduction models constrained by deep earthquakes beneath the Japan Sea and eastern China. *Scientific Reports*, *10*(1), 5440. https://doi.org/10.1038/s41598-020-62238-x

Dong, W., Glazyrin, K., Khandarkhaeva, S., Fedotenko, T., Bednarčík, J., Greenberg, E., et al. (2022). $Fe_{0.79}Si_{0.07}B_{0.14}$ metallic glass gaskets for high-pressure research beyond 1 Mbar. *Journal of Synchrotron Radiation*, *29*(5), 1167–1179. https://doi.org/10.1107/S1600577522007573

Fei, Y., Ricolleau, A., Frank, M., Mibe, K., Shen, G., & Prakapenka, V. (2007). Toward an internally consistent pressure scale. *Proceedings of the National Academy of Sciences of the United States of America*, *104*(22), 9182–9186. https://doi.org/10.1073/pnas.0609013104

Fischer, R. A., Campbell, A. J., Chidester, B. A., Reaman, D. M., Thompson, E. C., Pigott, J. S., et al. (2018). Equations of state and phase boundary for stishovite and $CaCl_2$-type SiO_2. *American Mineralogist*, *103*(5), 792–802. https://doi.org/10.2138/am-2018-6267

Girard, J., Amulele, G., Farla, R., Mohiuddin, A., & Karato, S. (2016). Shear deformation of bridgmanite and magnesiowüstite aggregates at lower mantle conditions. *Science*, *351*(6269), 144–147. https://doi.org/10.1126/science.aad3113

Helffrich, G., Ballmer, M. D., & Hirose, K. (2018). Core-exsolved SiO_2 dispersal in the Earth's mantle. *Journal of Geophysical Research: Solid Earth*, *123*(1), 176–188. https://doi.org/10.1002/2017JB014865

Hirose, K., Morard, G., Sinmyo, R., Umemoto, K., Hernlund, J., Helffrich, G., & Labrosse, S. (2017). Crystallization of silicon dioxide and compositional evolution of the Earth's core. *Nature*, *543*(7643), 99–102. https://doi.org/10.1038/nature21367

Hirose, K., Takafuji, N., Sata, N., & Ohishi, Y. (2005). Phase transition and density of subducted MORB crust in the lower mantle. *Earth and Planetary Science Letters*, *237*(1–2), 239–251. https://doi.org/10.1016/j.epsl.2005.06.035

Immoor, J., Miyagi, L., Liermann, H.-P., Speziale, S., Schulze, K., Buchen, J., et al. (2022). Weak cubic $CaSiO_3$ perovskite in the Earth's mantle. *Nature*, *603*(7900), 276–279. https://doi.org/10.1038/s41586-021-04378-2

Ishii, T., Kojitani, H., & Akaogi, M. (2019). Phase relations of harzburgite and MORB up to the uppermost lower mantle conditions: Precise comparison with pyrolite by multisample cell high-pressure experiments with implication to dynamics of subducted slabs. *Journal of Geophysical Research: Solid Earth*, *124*(4), 3491–3507. https://doi.org/10.1029/2018JB016749

Ishii, T., Miyajima, N., Criniti, G., Hu, Q., Glazyrin, K., & Katsura, T. (2022). High pressure-temperature phase relations of basaltic crust up to mid-mantle conditions. *Earth and Planetary Science Letters*, *584*, 117472. https://doi.org/10.1016/j.epsl.2022.117472

Kaneshima, S. (2019). Seismic scatterers in the lower mantle near subduction zones. *Geophysical Journal International*, *219*(1), S2–S20. https://doi.org/10.1093/gji/ggz241

Kaneshima, S., & Helffrich, G. (2010). Small scale heterogeneity in the mid-lower mantle beneath the circum-Pacific area. *Physics of the Earth and Planetary Interiors*, *183*(1–2), 91–103. https://doi.org/10.1016/j.pepi.2010.03.011

Kirby, S. H., Stein, S., Okal, E. A., & Rubie, D. C. (1996). Metastable mantle phase transformations and deep earthquakes in subducting oceanic lithosphere. *Reviews of Geophysics*, *34*(2), 261–306. https://doi.org/10.1029/96RG01050

Lakshtanov, D. L., Sinogeikin, S. V., Litasov, K. D., Prakapenka, V. B., Hellwig, H., Wang, J., et al. (2007). The post-stishovite phase transition in hydrous alumina-bearing SiO_2 in the lower mantle of the Earth. *Proceedings of the National Academy of Sciences of the United States of America*, *104*(34), 13588–13590. https://doi.org/10.1073/pnas.0706113104

Liermann, H.-P., Konôpková, Z., Morgenroth, W., Glazyrin, K., Bednarčík, J., McBride, E. E., et al. (2015). The extreme conditions beamline P02.2 and the extreme conditions science infrastructure at PETRA III. *Journal of Synchrotron Radiation*, *22*(4), 908–924. https://doi.org/10.1107/S1600577515005937

Litasov, K. D., & Ohtani, E. (2005). Phase relations in hydrous MORB at 18–28 GPa: Implications for heterogeneity of the lower mantle. *Physics of the Earth and Planetary Interiors*, *150*(4), 239–263. https://doi.org/10.1016/j.pepi.2004.10.010

Marquardt, H., Buchen, J., Mendez, A. S. J., Kurnosov, A., Wendt, M., Rothkirch, A., et al. (2018). Elastic softening of $(Mg_{0.8}Fe_{0.2})O$ ferropericlase across the iron spin crossover measured at seismic frequencies. *Geophysical Research Letters*, *45*(14), 6862–6868. https://doi.org/10.1029/2018GL077982

Marquardt, H., Gleason, A., Marquardt, K., Speziale, S., Miyagi, L., Neusser, G., et al. (2011). Elastic properties of MgO nanocrystals and grain boundaries at high pressures by Brillouin scattering. *Physical Review B*, *84*(6), 064131. https://doi.org/10.1103/PhysRevB.84.064131

Marquardt, H., & Marquardt, K. (2012). Focused ion beam preparation and characterization of single-crystal samples for high-pressure experiments in the diamond-anvil cell. *American Mineralogist*, *97*(2–3), 299–304. https://doi.org/10.2138/am.2012.3911

Marquardt, H., Speziale, S., Marquardt, K., Reichmann, H. J., Konôpková, Z., Morgenroth, W., & Liermann, H.-P. (2011). The effect of crystallite size and stress condition on the equation of state of nanocrystalline MgO. *Journal of Applied Physics*, *110*(11), 113512. https://doi.org/10.1063/1.3662491

Marquardt, H., & Thomson, A. R. (2020). Experimental elasticity of Earth's deep mantle. *Nature Reviews Earth & Environment*, *1*(9), 455–469. https://doi.org/10.1038/s43017-020-0077-3

McKnight, R. E. A., Moxon, T., Buckley, A., Taylor, P. A., Darling, T. W., & Carpenter, M. A. (2008). Grain size dependence of elastic anomalies accompanying the α–β phase transition in polycrystalline quartz. *Journal of Physics: Condensed Matter*, *20*(7), 075229. https://doi.org/10.1088/0953-8984/20/7/075229

Méndez, A. S. J., Marquardt, H., Husband, R. J., Schwark, I., Mainberger, J., Glazyrin, K., et al. (2020). A resistively-heated dynamic diamond anvil cell (RHdDAC) for fast compression X-ray diffraction experiments at high temperatures. *Review of Scientific Instruments*, *91*(7), 073906. https://doi.org/10.1063/5.0007557

Méndez, A. S. J., Stackhouse, S., Trautner, V., Wang, B., Satta, N., Kurnosov, A., et al. (2022). Broad elastic softening of (Mg,Fe)O ferropericlase across the iron spin crossover and a mixed-spin lower mantle. *Journal of Geophysical Research: Solid Earth*, *127*(8), e2021JB023832. https://doi.org/10.1029/2021JB023832

Méndez, A. S. J., Trybel, F., Husband, R. J., Steinle-Neumann, G., Liermann, H.-P., & Marquardt, H. (2021). Bulk modulus of H_2O across the ice VII–ice X transition measured by time-resolved x-ray diffraction in dynamic diamond anvil cell experiments. *Physical Review B*, *103*(6), 064104. https://doi.org/10.1103/PhysRevB.103.064104

Nishiyama, N., Wakai, F., Ohfuji, H., Tamenori, Y., Murata, H., Taniguchi, T., et al. (2015). Fracture-induced amorphization of polycrystalline SiO_2 stishovite: A potential platform for toughening in ceramics. *Scientific Reports*, *4*(1), 6558. https://doi.org/10.1038/srep06558

Nomura, R., Hirose, K., Sata, N., & Ohishi, Y. (2010). Precise determination of post-stishovite phase transition boundary and implications for seismic heterogeneities in the mid-lower mantle. *Physics of the Earth and Planetary Interiors*, *183*(1–2), 104–109. https://doi.org/10.1016/j.pepi.2010.08.004

Prescher, C., & Prakapenka, V. B. (2015). *DIOPTAS*: A program for reduction of two-dimensional X-ray diffraction data and data exploration. *High Pressure Research*, *35*(3), 223–230. https://doi.org/10.1080/08957959.2015.1059835

Shieh, S. R., Duffy, T. S., & Li, B. (2002). Strength and elasticity of SiO_2 across the stishovite–$CaCl_2$-type structural phase boundary. *Physical Review Letters*, *89*(25), 255507. https://doi.org/10.1103/PhysRevLett.89.255507

Singh, A. K. (2004). X-ray diffraction from solids under nonhydrostatic compression—Some recent studies. *Journal of Physics and Chemistry of Solids*, *65*(8–9), 1589–1596. https://doi.org/10.1016/j.jpcs.2003.11.044

Singh, A. K., Andrault, D., & Bouvier, P. (2012). X-ray diffraction from stishovite under nonhydrostatic compression to 70 GPa: Strength and elasticity across the tetragonal → orthorhombic transition. *Physics of the Earth and Planetary Interiors*, *208–209*, 1–10. https://doi.org/10.1016/j.pepi.2012.07.003

Singh, A. K., Balasingh, C., Mao, H., Hemley, R. J., & Shu, J. (1998). Analysis of lattice strains measured under nonhydrostatic pressure. *Journal of Applied Physics*, *83*(12), 7567–7575. https://doi.org/10.1063/1.367872

Singh, A. K., & Kenichi, T. (2001). Measurement and analysis of nonhydrostatic lattice strain component in niobium to 145 GPa under various fluid pressure-transmitting media. *Journal of Applied Physics*, *90*(7), 3269–3275. https://doi.org/10.1063/1.1397283

Singh, A. K., Liermann, H. P., Saxena, S. K., Mao, H. K., & Devi, S. U. (2006). Nonhydrostatic compression of gold powder to 60 GPa in a diamond anvil cell: Estimation of compressive strength from X-ray diffraction data. *Journal of Physics: Condensed Matter*, *18*(25), S969–S978. https://doi.org/10.1088/0953-8984/18/25/S05

Tan, E., Gurnis, M., & Han, L. (2002). Slabs in the lower mantle and their modulation of plume formation. *Geochemistry, Geophysics, Geosystems*, *3*(11), 1–24. https://doi.org/10.1029/2001GC000238

Thielmann, M., Golabek, G. J., & Marquardt, H. (2020). Ferropericlase control of lower mantle rheology: Impact of phase morphology. *Geochemistry, Geophysics, Geosystems*, *21*(2), e2019GC008688. https://doi.org/10.1029/2019GC008688

Toby, B. H., & Von Dreele, R. B. (2013). GSAS-II: The genesis of a modern open-source all purpose crystallography software package. *Journal of Applied Crystallography*, *46*(2), 544–549. https://doi.org/10.1107/S0021889813003531

Wang, B. (2022). Batch peaks fitting script in Python for time-resolved XRD data analysis (version v1.0.0). *Zenodo*. https://doi.org/10.5281/ZENODO.7457445

Wirth, R., Vollmer, C., Brenker, F., Matsyuk, S., & Kaminsky, F. (2007). Inclusions of nanocrystalline hydrous aluminium silicate "Phase Egg" in superdeep diamonds from Juina (Mato Grosso State, Brazil). *Earth and Planetary Science Letters*, *259*(3–4), 384–399. https://doi.org/10.1016/j.epsl.2007.04.041

Yang, R., & Wu, Z. (2014). Elastic properties of stishovite and the $CaCl_2$-type silica at the mantle temperature and pressure: An ab initio investigation. *Earth and Planetary Science Letters*, *404*, 14–21. https://doi.org/10.1016/j.epsl.2014.07.020

Yeheskel, O., Chaim, R., Shen, Z., & Nygren, M. (2005). Elastic moduli of grain boundaries in nanocrystalline MgO ceramics. *Journal of Materials Research*, *20*(3), 719–725. https://doi.org/10.1557/JMR.2005.0094

Zhang, Y., Fu, S., Karato, S., Okuchi, T., Chariton, S., Prakapenka, V. B., & Lin, J. (2022). Elasticity of hydrated Al-bearing stishovite and post-stishovite: Implications for understanding regional seismic V_S anomalies along subducting slabs in the lower mantle. *Journal of Geophysical Research: Solid Earth*, *127*(4), e2021JB023170. https://doi.org/10.1029/2021JB023170

Zhang, Y., Fu, S., Wang, B., & Lin, J.-F. (2021). Elasticity of a pseudoproper ferroelastic transition from stishovite to post-stishovite at high pressure. *Physical Review Letters*, *126*(2), 025701. https://doi.org/10.1103/PhysRevLett.126.025701

Zhu, L., & Zheng, X. (2010). Influence of interface energy and grain boundary on the elastic modulus of nanocrystalline materials. *Acta Mechanica*, *213*(3–4), 223–234. https://doi.org/10.1007/s00707-009-0263-3